PAPER • OPEN ACCESS

X-ray radiography of microjetting from grooved surfaces in tin sample subjected to laser driven shock

To cite this article: Jianting Xin *et al* 2019 *J. Micromech. Microeng.* **29** 095011

View the article online for updates and enhancements.

X-ray radiography of microjetting from grooved surfaces in tin sample subjected to laser driven shock

Jianting Xin[1,6], **Anmin He**[2,6], **Wenbin Liu**[2,3,4], **GenBai Chu**[1], **Minghai Yu**[1], **Wei Fan**[1], **YuChi Wu**[1], **Tao Xi**[1], **Min Shui**[1], **Yongqiang Zhao**[1], **Pei Wang**[2], **Yuqiu Gu**[1] and **Weihua He**[1,5]

[1] Science and Technology on Plasma Physics Laboratory, Research Center of Laser Fusion, China Academy of Engineering Physics, PO Box 919-986, Mianyang, 621900, People's Republic of China
[2] Institute of Applied Physics and Computation Mathematics, Beijing 100088, People's Republic of China
[3] Graduate School of China Academy of Engineering Physics, Beijing 100088, People's Republic of China
[4] Department of Modern Mechanics, University of Science and Technology of China, Hefei 230026, People's Republic of China

E-mail: heweihua2004@sina.com

Abstract

When a triangular shock wave reflects from the free surface of a solid sample, microjetting may emit from the grooved surface, leading to high velocity approximately micrometer-size fragments. Microjetting is an important issue for material dynamic response under shock loading in both fundamental science and practical applications. In this paper, the dynamic process of microjetting is investigated in the laser-driven shock loading conditions, the experiments were performed at the ShenguangII-U (SGII-U) laser facility. Microjetting from the triangular grooves in the free surface of a tin sample is diagnosed with x-ray radiography, where the 40–200 keV high energy x-ray is created with the picosecond laser beam focused on a Au μ-wire target. The density distribution along the microjetting and cumulated mass can be inferred from the images radiographied by such ultrashot high energy x-ray. The density distribution shows two representative regions including the head region of microjetting with low density and high speed, and the root region with high density and low speed. The microjets from three continuous parallel grooves with 60° angle are significantly different from that of 120° angle, the effect of the groove angle was verified by numerical simulation and experimental results.

Keywords: x-ray radiography, microjetting, laser shock loading, grooves

(Some figures may appear in colour only in the online journal)

---

[5] Author to whom any correspondence should be addressed.
[6] Jianting Xin and Anmin He contributed equally to this article.

1. Introduction

It has been known for a long time that the breakout and reflection of a strong shock wave from the material free surface may lead to ejection [1–3]. Extensive experimental and theoretical studies have shown that the mechanism of ejecta formation is very complicated, and the mass, size, shape and velocity of ejecta vary depending on the initial shock conditions and the surface defects of the material [4–6]. In practice, the material surface is not an ideal plane due to the existence of surface defects such as scratches and grooves. These surface defects may lead to the ejection of micro-scale material, and the velocity of the microjetting is much faster than that of free surface. This process has been extensively studied under explosive and plate impact. For instance, Asay *et al* investigated the total ejected mass and its distribution by developing thin-foil and thick-plate techniques [7]. Meanwhile, numerous diagnostic techniques like the line holography, proton radiography, optical shadowgraph and photonic Doppler velocimetry, have been developed and adopted to study the microjetting process [8–10].

In recent decades, lasers have provided a promising shock loading technique for investigating the process of microjetting under extreme condition applications of high strain rate [11]. When a high-power laser pulse is focused onto a metal target, the plasma formed by the laser ablation expands outward, which drives a shock wave into the target. The release wave from the loaded surface following the shock wave produces a triangular shock pulse. When the shock wave reflects from the target's free surface, scratches and defects in the surface may lead to microjetting. Rességuier *et al* has carried out experimental and theoretical research on microjetting under laser shock loading and has analyzed fragment size with soft recovery technique and modeling issues [12–15]. Our group also have performed the dynamic fragmentation experiments at Shenguang-Ⅲ (SGⅢ) prototype laser facility, the fragments under sequential loading pressures were recovered by Poly 4-methyl-1-pentene (PMP) foam, and the size, shape and penetration depth of the fragments were analyzed by x-ray micro-tomography and the improved watershed method [16, 17]. Although the soft recovery and post-examination of the recovered sample can provide clear images for globally visualizing the fragments, important data on ejection properties, such as its velocity and density distribution, could not be obtained. By contrast, x-ray radiography provides a more powerful means for measuring the evolution of microjetting. Moreover, owing to its inherent advantage over optical imaging systems, it can quantitatively determine material densities by measuring the x-ray transmission [3, 8, 18]. However, there are only a few report on microjetting density measurements, due to its great challenge in dynamic diagnostics of microjetting process by x-ray radiography. Recently, Rességuier *et al* [19] reported on an experiment of x-ray radiography of the microjetting driven by laser, and the x-ray generated by picosecond laser irradiation of a thin copper wire. The density gradients along the microjetting and the total ejected mass were estimated, which is helpful to understand the properties of microjetting.
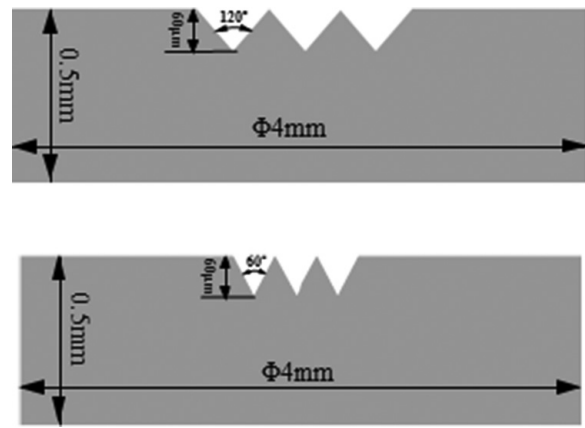

Figure 1. Schematic of cross sections of Tin samples with grooves of 30° and 60° half-angles.
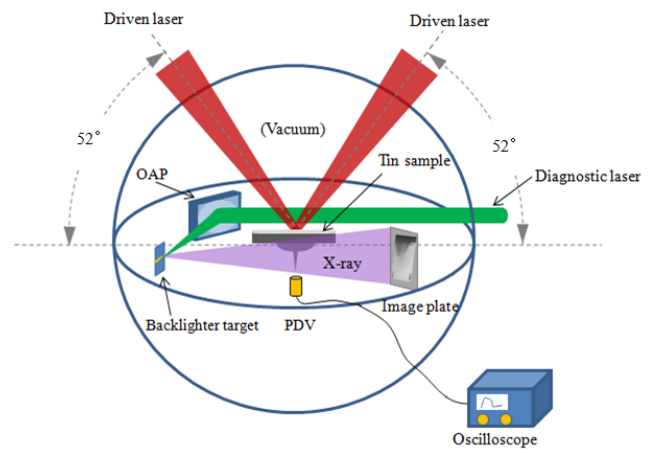

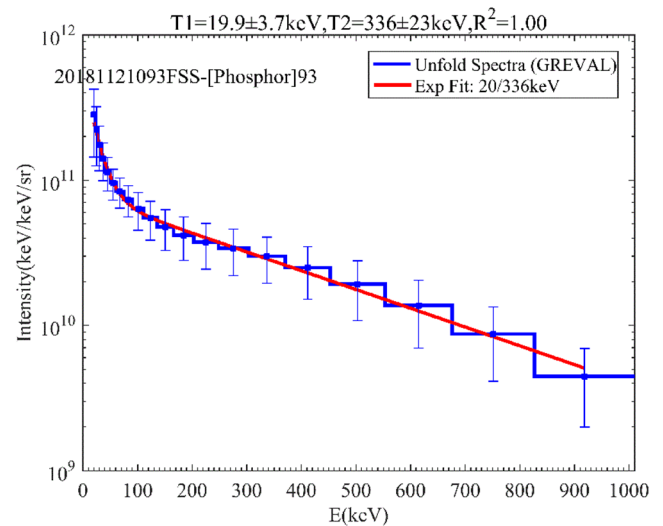**Figure 2.** Schematic of the experimental setup.

Figure 3. Bremsstrahlung spectrum obtained and its exponential fitting.

In this paper, our group have explored x-ray radiography of microjetting from the grooved surface of a tin sample driven by nanosecond pulse laser, and the 40–200 kev high energy x-ray is created with the picosecond laser beam focused on a

Table 1. Laser loading parameters, the measured free surface velocities, the corresponding calculated free surface pressure and microjet tip velocities.

Shot No.	Laser energy (J)	Grooves angle	Peak velocity of free surface (kms^{-1})	Pressure near free surface (GPa)	Delay time of ps laser with respect to driven laser pulse	Microjet tip velocities (kms^{-1})
Shot 1	771	120°	1.92	29.1	300ns	3.5
Shot 2	618	120°	1.66	25	600ns	3
Shot 3	658	60°	1.81	26.2	300ns	3.3
Shot 4	641	60°	1.78	25.7	600ns	3.3

Au μ-wire target. The areal density distribution of microjetting inferred from the recorded radiographic images by means of step wedge comparison and the cumulated mass and the effect of groove angle are analyzed.

2. Sample preparation

The samples in our experiment are high purity Tin, with a thickness of 500 μm. The samples' surfaces were polished with the random roughness of 40 nm Ra. Three straight continuous parallel grooves were machined in the middle of the samples' free surface, the grooves were V-shaped and about 60 μm deep. Two types of tin samples, shown in figure 1, were explored in the experiment, one has machined grooves in the tin surface with half-angles of 60° and the other has machined grooves with half-angles of 30°.

3. Experimental setup

The experiments were performed on the SGII-U laser facility, and the setup is schematically represented in figure 2.

Two of eight driven laser beams with 0.351 μm wavelength, and 3 ns duration, are focused onto the target at 52° angle. The beams are smoothed by continuous phase plates (CPP) and the irradiated spot is quasi circular with about 2 mm diameter at the sample surface, and the grooved surface is opposite to the irradiated spot. The total energy of the two beams can be adjusted from 100 J to 1400 J. Preliminary computations of laser-matter interaction and shock wave propagation in the tin sample are performed with a 1D Lagrangian hydrodynamics and energy transport code and material data of tin from the SESAME tables. The pressure history along the propagation distance from the irradiated surface and the pressure near the free surface of sample can be evaluated. In the experiment a fiber-optics probe of photonic Doppler velocimetry (PDV) was located just below the tin sample to monitor the velocity of the flat region outside of grooves of the sample surface.

In the experiments, the driven laser pulses drive a shock wave in the tin sample. The ejection of micron-scale material would be expected to be emitted from the grooves in the free surface of the shocked sample. The ps laser pulse of SGII-U with ~10 ps duration, and about 500 J was used as the diagnostic laser beam. Such a short laser pulse was focused onto a 300 × 10 × 10 μm Au μ-wire backlight target to generate high energy x-ray source for radiography at a certain time delay after the driven laser pulses. The x-ray spectrum was
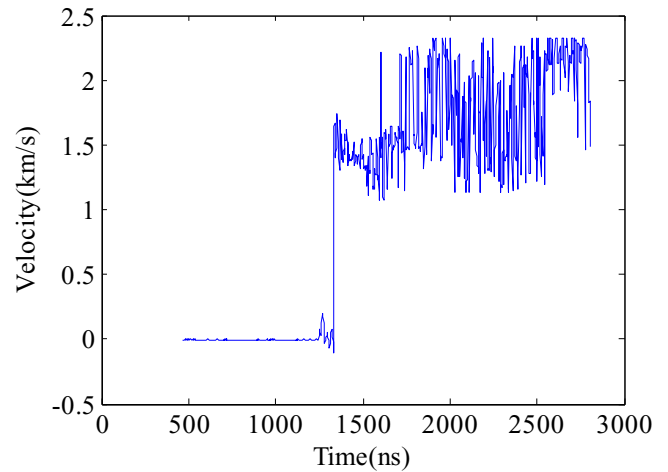
Figure 4. Velocity history for the Shot 2 measured from PDV.

monitored using a filter stack spectrometer, figure 2 shows the typical measurement of the x-ray bremsstrahlung spectra in the experiments, which is 20 keV–1 MeV. The x-ray propagates through the tin sample and the microjettings along the groove direction, an image plate was put behind the sample to record the microjectting radiographic image (shown in figure 2). In our experiments, the x-ray lower than 40 keV was filtered by a copper foil with 500 μm thickness in front of the IP, while the x-ray higher than 200 keV filter was cut off for the highest spectrum response of IP. As a result, the spectra of interest for the detected x-ray radiograph was limited within 40–200 keV. The bremsstrahlung spectrum obtained in the experiment and its exponential fitting is shown in figure 3. More details about the back light can be found in [20].

The distance between the tin target and image plate was set to about 13 mm, the obtained image was magnified by about 37.5 times. Step wedges consisting of Sn and of thicknesses between 0.15 and 2 mm were stuck on the front of the IP.

4. Experiment results and analysis

X-ray radiography experiments were performed on each type of tin samples for two shots, the expected energy of the driven laser was set as 700 J. However, in the experiment, the energy had fluctuations of 10% from shot to shot. The actual energy was measured by the energy meter in real time. Two x-ray radiographic images were recorded for each type of tin sample at the delay times of 300 ns and 600 ns after the driven laser pulse, respectively. The laser loading parameters for the
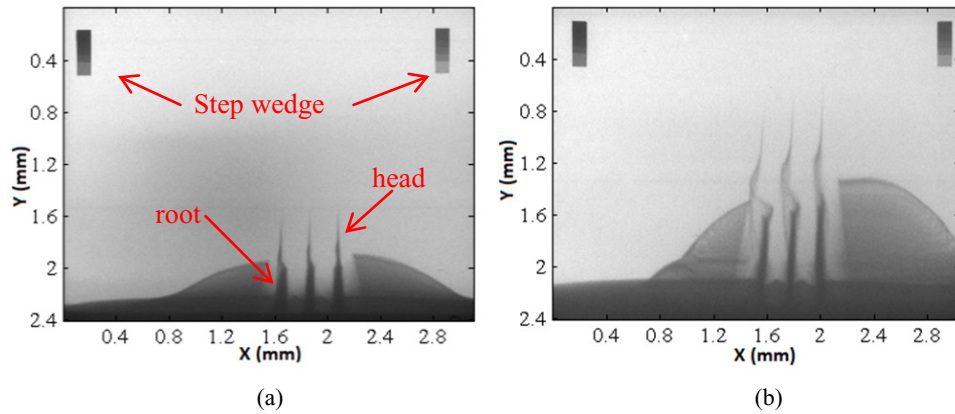
Figure 5. Radiography results of tin microejection in shot 1 and shot 2. (a) Shot 1, (b) shot 2.
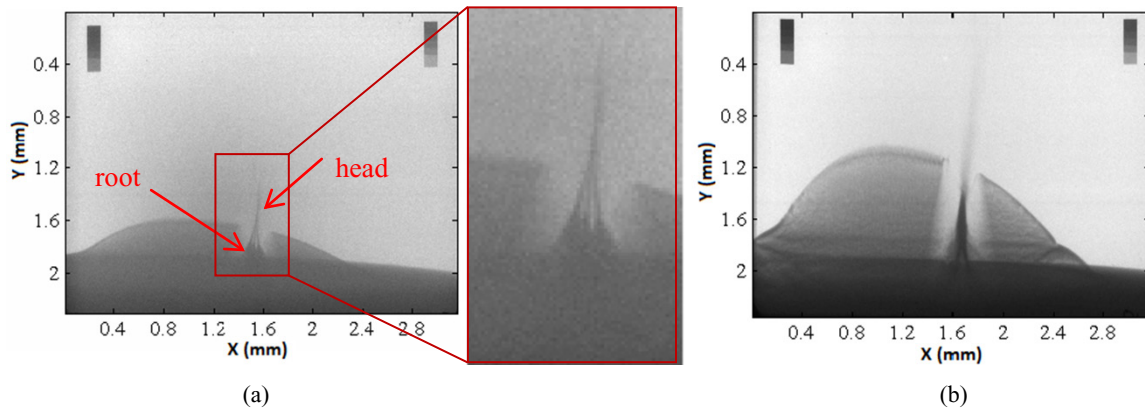

Figure 6. Radiography results of tin microejection in shot 3 and shot 4. (a) Shot 3, (b) shot 4.

four shots and the peak velocity of the samples' free surface measured by PDV are shown in table 1. According to the measured velocities, the loading pressures near free surface were calculated, which were also shown in the same table. Figure 4 shows a typical velocity history for shot 2 from the PDV measurement.

The pressures near the tin samples' free surface of these four shots vary with the loading laser energy, the samples should be in a partially melted state under such loading pressures.

Figure 5 shows x-ray radiographic images of shot 1 and shot 2, in these two shots, the first type of tin sample was used, which had machined grooves in tin surface of 60° half angle.

Microjettings from three grooves are clearly observed in figure 5(a), each microjetting consists of a head and a root with carrot forming, the three microjets are separate. In addition, the pixels of their head have high gray-scale value, indicating the low density. Compared with the head, the root of the microjet is expected to have higher density from its low gray-scale value. Under similar loading parameters, x-ray radiography image of microjet on 600ns time delay after driven laser is shown in figure 5(b). The conformation of three microjets was similar to the microjets in figure 5(a), which consists of a head and foot, the length of the head and the root augmented for a longer spray time compare with figure 5(a) and the gray-scale value of the head goes up owing to ejecta of the head distributing more sparsely.

Figure 6 shows x-ray radiographic images of shot 3 and shot 4, in these two shots, the second type of tin sample was

used, which had machined grooves with half angle of 30°. For shot 3, three microjets from grooves converge at the position of the head, though the features of the microjets are similar to that of shot 1 and 2, which consists of head and root. For the grooves in the sample with 30° half angle, shock waves breakout at the grooves surface, the brink of bilateral grooves moved inward, the bilateral microjets from the two grooves squeeze inward, which makes the three microjets converge. The three microjets converge at the head region initially and finally converge completely for the whole region, as shown in the figure 6(b), the roots of these microjets converge to form one spike.

From the radiographic images, it can be found that the speed of the microjet tips are significantly faster than that of free surface, and the speed of microjet tips of the four shots, estimated from the images, are shown in table 1, which are all about 1.8 times the corresponding free surface's velocity. Such phenomenon has been verified by many research works. For example, as early as in 1982, Andriot *et al* [21] observed that the ejected particle velocity was almost twice the free surface by measuring ejected mass flux of lead-alloy with a Doppler laser interferometry technique.

5. Mass areal density and total mass of microjetting

The mass areal density of the x-ray radiography images is inferred from step wedges shown in figure 7. The mass areal
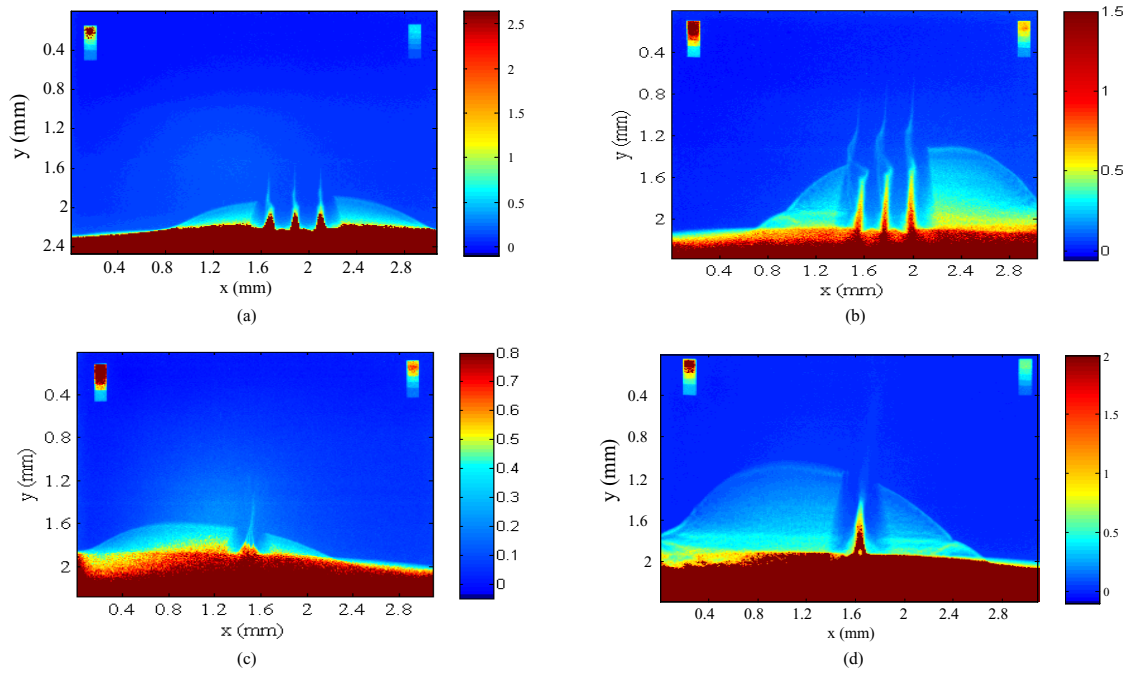
Figure 7. Calculated areal density results. (a) Shot 1, (b) shot 2, (c) shot 3, (d) shot 4.

density of the root of microjet is much higher than that of the head, and in shot 1 (figure 7(a)) and 4 (figure 7(d)), the mass density of the root cannot be estimated quantitively, for the photon energy of the x-ray is not high enough to penetrate. With a longer spray time shown as in figure 7(b), the roots grow up to spikes, and the mass areal density increased gradually from the tip to the bottom, and the bottom of the spikes in depth to the sample.

The mass areal density distribution and cumulated mass distribution along microjet direction of each microjetting was analyzed. Figure 8 is the illustration of the analysis of right microjet in shot 2.

The total mass of the microjets in our experiments was calculated and is shown in table 2. The total mass here is the total amount of ejecta above the free surface. For shot 1 and 2, the total mass of each microjet was calculated, and the three microjets' masses are consistent in one shot. In shot 3 and 4, we calculated the total mass in the three jets after they converge. For the two types of grooved sample, the total mass of ejecta increased with time shift from 300 ns to 600 ns, it also could be found that the microjet mass increases with the vertex half-angle of grooves which is in agreement with the experimental results of Zellner [4, 6]. Jetting factor, defined by Asay and Bertholf [22], is 4 in shot 2 for 60° half angle grooves and 4.6 in shot 4 for 30° half angle grooves.

6. Simulation analysis

6.1. Simulation of microjetting and estimation of total mass in the jets

We now turn to the modeling of the microjetting process using the independently developed 2D SPH code by Wang *et al* [23, 24]. Preliminary computations of laser-matter interaction
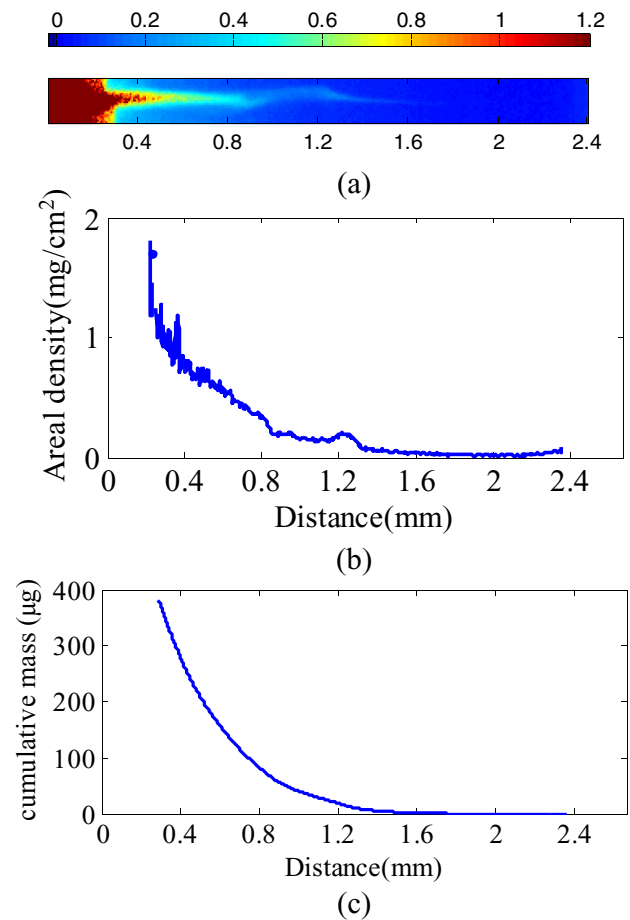

Figure 8. Illustration of radiography analysis for microjet of shot 2. (a) Areal density image of microjet (b) mass areal density distribution in the microjet; (c) cumulated mass distribution along microjet direction.

Table 2. The total mass of microjets.

Shot No.	Laser power (J)	Half angle of grooves	Delay time of ps laser with respect to driven laser pulse	Microjet mass (mg)		
				Left	Middle	Right
Shot 1	771	60°	300ns	0.14	0.12	0.15
Shot 2	618	60°	600ns	0.37	0.33	0.36
Shot 3	658	30°	300ns		0.16	
Shot 4	641	30°	600ns		0.42	

and shock wave propagation in the tin sample are performed with a 1D Lagrangian hydrodynamics and energy transport code and material data of tin from the SESAME tables. The tin sample is modeled using metallic polynomial equation of state, Steinberg–Guinan constitutive model and Lindeman melting law [25]. A P_{min} spall damage model is adopted, i.e. the tin spalls when the pressure within the material is less than $P \leqslant P_{min} = -1.2 GPa$. This value was chosen according to the data in Kanel [26]. After the tin melts, its spall strength is set to $-0.1 GPa$. For $19.5\ Gpa \leqslant P_{sb} \leqslant 33 GPa$, the tin releases to the mixed solid–liquid phase [27], the metallic polynomial equation of state cannot accurately reflect this state, and the particle break up model cannot reflect the real physical destruction well. For these reasons, the calculation is clearly not good enough to reproduce many of the observed details of the experiment, but the general features seem to agree quite well.

Simulation result of microjettings from grooves at 600 ns after laser shock are shown in figure 10. The form and internal structure of microjettings from the two types of grooves are in quite good agreement with the experiments, each microjetting consists of the head with low density and the foot with high density. The tip velocity of microjetting from the groove with 60° half angle simulated to be 3.01 km s^{-1}, which is in agreement with the measured 3.0 km s^{-1} in experiment.

The simulation tip velocity of microjetting form 30° half angle groove is 4.02 km s^{-1} and is a little faster than the velocity measured in the experiment, a possible reason for this is the collision of the head of three microjettings, which made the deceleration.

The cumulated mass along microjetting can be evaluated from the simulation result of volume density distribution. Figure 10(a) gives its simulation result of the middle microjetting that is shown in figure 9(a). The related cumulated mass from simulation and experiment are in good agreement, as shown in figure 10(b).

6.2. Analysis of microjettings from grooves with half angle of 30° and 60°

The pressure distribution and the velocity distribution perpendicular to the shock direction in two types of sample at different times are simulated, to analyze the mechanism by which groove angle influences the convergence of the
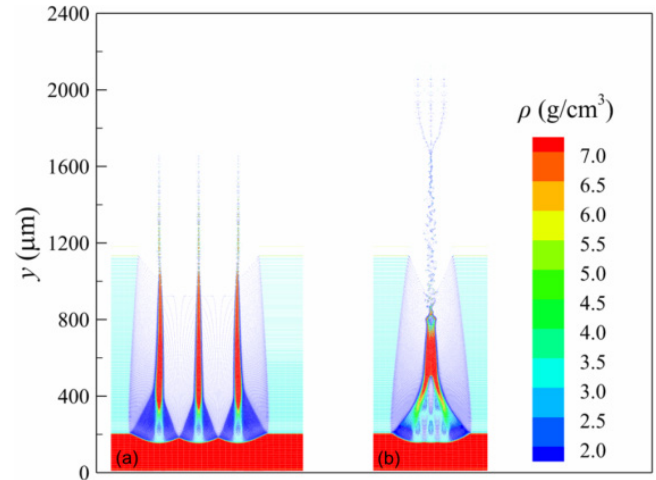

Figure 9. SPH simulation of microjetting from two types of grooves at 600ns after laser shock: (a) grooves of 60° half angle, (b) grooves of 30° half angle.

microjets in the experiments. In figure 11, after the incident shocks were reflected from the groove surface and free surface, the pressure and velocity distribution on both sides of side grooves are asymmetric because of the geometric asymmetry, however, the asymmetry is weak because of the long distance between the grooves and because the three microjets are separate. In figure 12, at 137 ns, the interaction of the incident shocks with groove surface at an incident angle 60° is irregular [11]. At this moment, the pressure and velocity distributions on both sides of three grooves are symmetric, and three microjets are separate. At 149 ns, the rarefaction wave that was reflected from the side groove and propagated inward met the rarefaction wave that was reflected from the middle groove and propagated outward, both are unloaded to zero, but the rarefaction wave that was reflected from the side groove and propagated outward is not affected and continues to propagate outward, therefore, the pressure distribution on both sides of the side grooves is asymmetric so that the pressure on the outside is greater than that on the inside. At 183 ns, because of the asymmetric distribution of the source material energy of peripheral microjets, the middle parts of peripheral microjets move toward the central microjets and converge eventually at 380 ns. As the density of front parts of three microjets is very small, these parts of the material are not obtained in experimental radiography results.
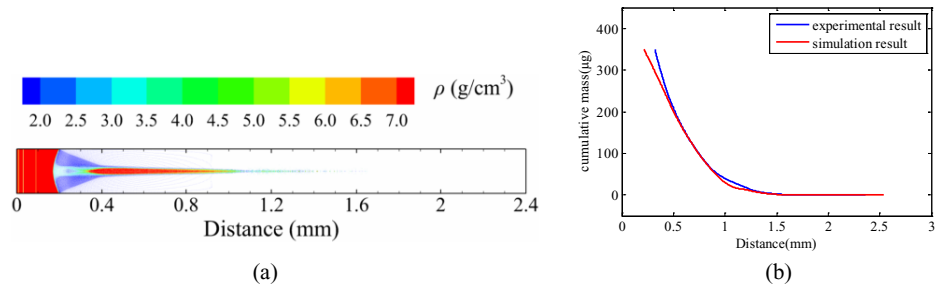
Figure 10. (a) Volume density distribution and cumulated mass of the middle microjetting from the 60° half-angle grooves. (b) Comparison of the cumulated mass from simulation and experiment.
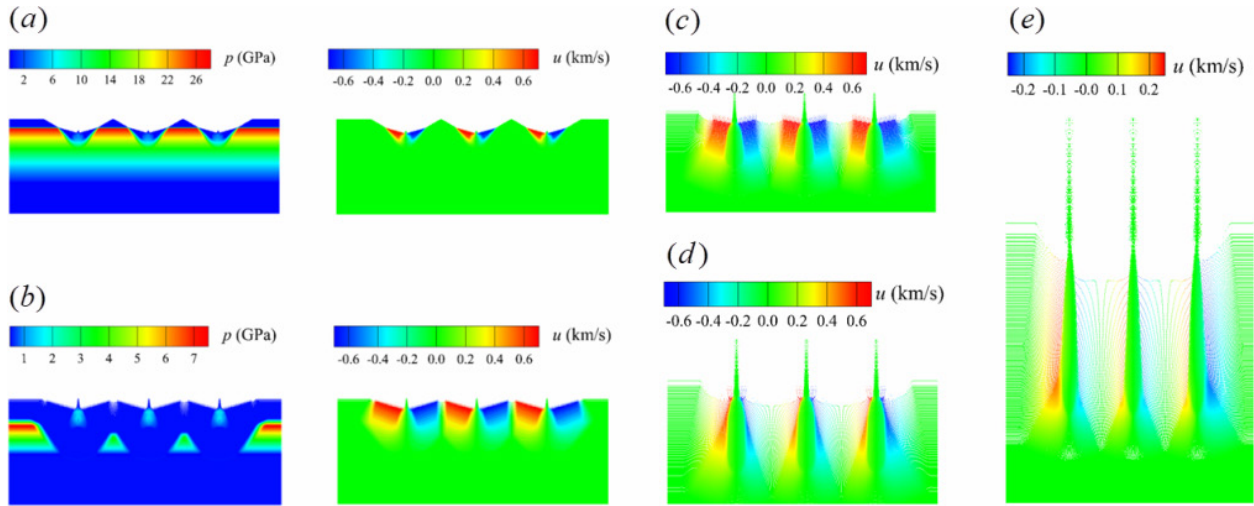

Figure 11. Pressure and velocity distribution perpendicular to the shock direction in the sample with 60° half angle grooves. (a) 137 ns, (b) 159 ns, (c) 206 ns, (d) 270 ns, (e) 470 ns.
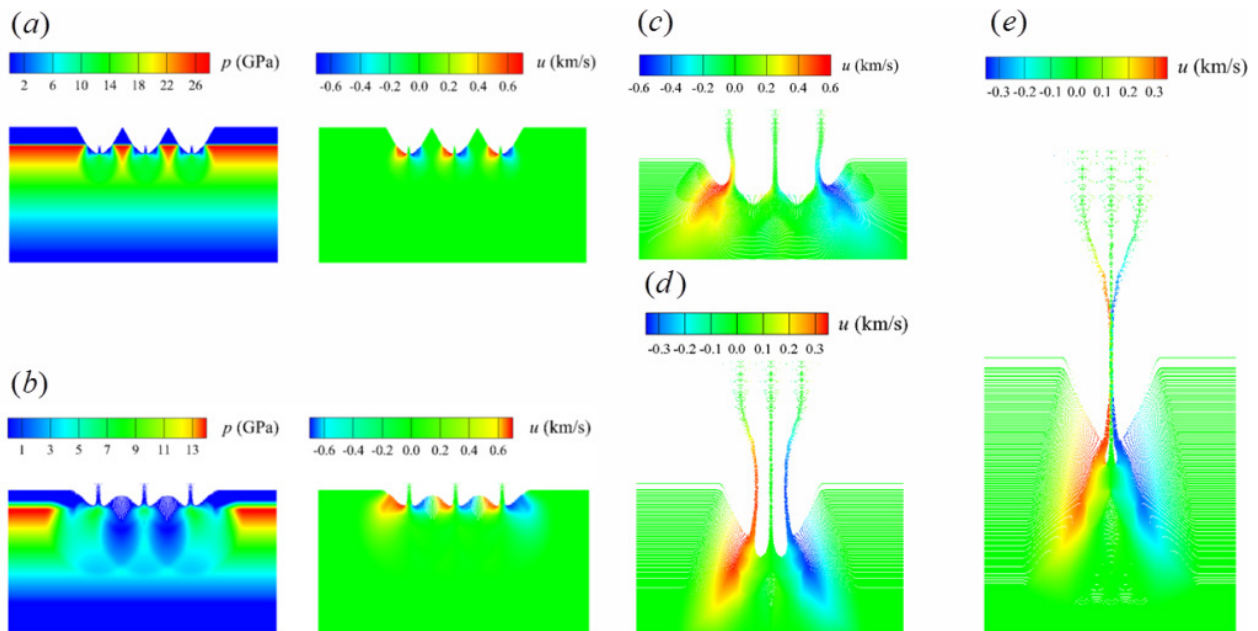

Figure 12. Pressure and velocity distribution perpendicular to the shock direction in the sample with 30° half angle grooves. (a) 137 ns, (b) 149 ns, (c) 183 ns, (d) 279 ns, (e) 380 ns.

7. Conclusion

Microjetting from triangular grooves of 60 μm depth with 30° and 60° half angle in tin sample was investigated under shock loading driven by nanosecond pulsed laser. A 40–200 keV high energy x-ray created by picosecond laser beam was employed to radiograph the microjetting process. The distinct images show that the microjet consists of a head with low density and a root with high density, the tip velocity of microjetting is nearly twice the velocity of the free surface. Simulation of the microjetting process by the 2D SPH code showed that the tip velocity and cumulated mass from simulation and experiment are in good agreement. The mechanism by which groove angle influences the convergence of microjets was analyzed.

Acknowledgments

ORCID iDs

Jianting Xin ⬤ https://orcid.org/0000-0003-4908-8114
Yuqiu Gu ⬤ https://orcid.org/0000-0001-6979-4556

References

[1] Walsh J M, Shreffler R G and Willig F J 1953 *J. App. Phys.* **24** 349
[2] Asay J R and Barker L M 1974 *J. Appl. Phys.* **45** 2540–6
[3] Ogorodnikov V A, Ivanov A G, Mikhailov A L, Kryukov N I, Tolochko A P and Golubev V A 1998 *Combust. Explos. Shock Waves* **34** 696
[4] Zellner M B *et al* 2007 *J. Appl. Phys.* **102** 013522
[5] Sorenson D S, Minich R W, Romero J L, Tunnell T W and Malone R M 2002 *J. Appl. Phys.* **92** 5830
[6] Zellner M B *et al* 2008 *J. Appl. Phys.* **103** 123502
[7] Asay J R 1978 *J. Appl. Phys.* **49** 6173
[8] Buttler W T *et al* 2009 *Proc. NEDPC LLNL (Livermore, CA, United States*, *26–30 October)* p 836
[9] Lescoute E, Rességuier T D, Chevalier J M, Loison D, Cuqlelandais J P, Boustie M, Breil J, Maire P H and Schurtz G 2010 *J. Appl. Phys.* **108** 093510
[10] Rességuier T D *et al* 2012 *Shock Compression Condens. Matter* **1462** 1015
[11] Rességuier T D, Lescoute E, Sollier A, Prudhomme G and Mercier P 2014 *J. Appl. Phys.* **115** 043525
[12] Signor L, Lescoute E, Loison D, Rességuier T D, Dragon A and Roy G 2010 *EPJ. Web Conf.* **6** 39012
[13] Signor L, Rességuier T D, Roy G, Dragon A and Llorca F 2007 *Shock Compression of Condensed Matter (Waikoloa, Hawaii*, *24–29 June)* p 593
[14] Rességuier T D, Signor L, Dragon A, Boustie M and Berthe L 2008 *Appl. Phys. Lett.* **92** 131910
[15] Signor L, Rességuier T D, Dragon A, Roy G, Fanget A and Faessel M 2010 *Int. J. Impact Eng.* **37** 887
[16] Xin J T, He W H, Shao J L, Li J, Wang P and Gu Y Q 2014 *J. Phys. D: Appl. Phys.* **47** 325304
[17] He W H *et al* 2014 *Opt. Express* **22** 18925
[18] Zhiembetov A K, Mikhaylov A L and Smirnov G S 2002 *AIP Conf. Proc.* **620** 547
[19] Rességuier T D, Prudhomme G, Roland C, Brambrink E, Loison D, Jodar B, Lescoute E and Sollier A 2018 *J. Appl. Phys.* **124** 06506
[20] Chu G *et al* 2018 *Rev. Sci. Ins.* **89** 115106
[21] Andriot P, Chapron P and Olive F 1981 *AIP Conf. Proc.* **78** 505
[22] Asay J R and Bertholf L D 1978 *Avail NTIS Energy Res. Abstr.* **4** 13928
[23] Wang P, Shao J L and Qin C S 2009 *Acta Phys. Sin* **58** 1064
[24] Wang P, Shao J L and Qin C S 2012 *Acta Phys. Sin* **61** 234701
[25] Liu W B, Ma D J, He A M and Wang P 2018 *Chin. Phys.* B **23** 047102
[26] Kanel G I, Savinykh A S, Garkushin G B and Razorenov S V 2015 *J. Exp. Theor. Phys. Lett.* **102** 615
[27] Monfared S K *et al* 2014 *J. Appl. Phys.* **116** 063504